Multistatic Noncoherent Linear Complexity Miller Sequence Detection For Gen2 RFID/IoT

Michail Ouroutzoglou, Georgios Vougioukas, George N. Karystinos and Aggelos Bletsas *Senior Member, IEEE*

***Abstract*—Passive Gen2 radio frequency identification (RFID) tags work thanks to the utilization of line codes that balance their operation between two opposite states: absorbing RF (for energy harvesting) and reflecting RF (for backscattering/communications). Given the current RF harvesting technology, batteryless tags need to be located very close to an active illuminator in order to harvest sufficient energy and operate. To tackle this limitation, prior art has tried to bring the illuminator closer to the tags by designing proprietary illuminating architectures. Our solution comes in two parts. First, we offer a novel, Gen2-compliant, near-optimal, noncoherent sequence detection algorithm with linear complexity (in the sequence length) for Miller line codes. We leverage the robustness of this algorithm to overcome issues inherent in multistatic setups, such as carrier frequency offset. Second, we propose a modular multistatic architecture that makes use of low-cost commodity software defined radios (SDR) and omnipresent Ethernet infrastructure. Simulations and experimental results in a monostatic, bistatic, or multistatic SDR testbed with commercial RFIDs, corroborate the low-cost, real-time and near-optimal flavor of our solution.**

***Index Terms*—Miller Coding, RFID, IoT, sequence detection, noncoherent detection, batteryless tags, multistatic reader.**

I. Introduction

Backscatter radio tags, such as those in radio frequency identification (RFID) and Internet-of-Things (IoT), have recently received a lot of positive attention. Their low-cost, ease of installation and batteryless character allows for wide and extensive deployment in various applications. Thus, this work seeks out ways to enhance the infrastructure that operates the tags, by introducing novel, real-time, near-optimal sequence detection algorithms, as well as methods to extend the operational range of such tags via multistatic radio.

The basic principle that these tags exploit is called backscattering, i.e. reflection radio. Backscattering is performed by alternating the terminating load of the tag's antenna between two different loads/states Z0 and Z1. Consequently, the tag's reflection coefficient is altered. For example, in state Z0, the antenna can be short-circuited, maximizing the amplitude of the reflection coefficient at the tag, while minimizing radio frequency (RF) energy harvesting. In state Z1, there is load matching, which minimizes the reflection coefficient and enables the tag to maximize energy absorption/harvesting from the impinging RF signal (Fig. 1). However, these two states do not correspond to logical "0" and "1"; instead there is added intelligence on the state transitioning, i.e., a line code.

The importance of line coding in batteryless tags stems from the need to alternate between the two contradicting states (energy reflection/absorption) on 50% duty cycle, independently of the data bits. Moreover, line codes introduce memory (and thus, added intelligence) on consecutive coded symbols. This allows the reader to better distinguish between noise and actual tag signal, reducing cases of *ghost* tag signals, i.e., misinterpretation of noise as useful tag information. This induced memory also offers coding gain, which in turn improves data detection. Available line codes in the industrial Gen2 RFID protocol include FM0 and Miller 2/4/8 [1].

In the industrial RFID Gen2 protocol [1], the RFID interrogation takes place during a slot in a framed slotted Aloha manner (see Fig. 2). Initially, the reader transmits a QUERY command that sets up communication parameters, such as tag rate, number of slots and tag line code (i.e., FM0 vs Miller). In turn, the tag generates and backscatters the RN16, i.e., a random 16-bit sequence. Then, the reader has to correctly receive the RN16 and acknowledge (ACK) it back to the tag. If the received ACK from the tag matches its transmitted RN16, then the tag backscatters a 128-bit data sequence, which includes the electronic product code (EPC) identification information (96 bits). Note that the tag appends a known preamble sequence at the start of every backscattered message, while there is option of activating an extra pilot (i.e., known) sequence, that could be further exploited (e.g., for channel estimation and respective coherent detection).

It is crucial to mention here that there is a strict timing constraint that needs to be taken into consideration when designing RFID readers and interrogation processes. This time constraint forces the reader to transmit the ACK within T_2 seconds after the RN16. Nominally, it holds that $\frac{3}{\mathrm{BLF}} \leq \mathrm{T}_2 \leq \frac{20}{\mathrm{BLF}}$, where BLF is the backscatter link frequency, set to $\mathrm{BLF} = 40\mathrm{KHz}$ for this work. This means that the reader has to transmit the ACK within $\mathrm{T}_2 = 500\mu\mathrm{s}$, otherwise the protocol times out. T_2 interval is highlighted in Fig. 2. Thus, interrogation processes, including detection algorithms, must be real-time and of limited complexity.

Now that we've explained the basic operation of passive Gen2 RFID tags, as well as some of the intricacies of the protocol, we discuss below ways to extend the interrogation range. Throughout the years, there have been many proposals, both by the industry and the research community, on how

Parts of this work are presented in [22] & [24]. This research has been cofinanced by the European Union and Greek national funds through the Operational Program Competitiveness, Entrepreneurship and Innovation, under the call RESEARCH - CREATE - INNOVATE (project code: T1EDK-03032). Authors are with School of ECE, Technical Univ. of Crete, Kounoupidiana Campus, Chania, Crete, Greece 73100. tel. +30-28210-37377, email: mouroutzoglou@isc.tuc.gr, gevougioukas@isc.tuc.gr, karystinos@telecom.tuc.gr, aggelos@telecom.tuc.gr

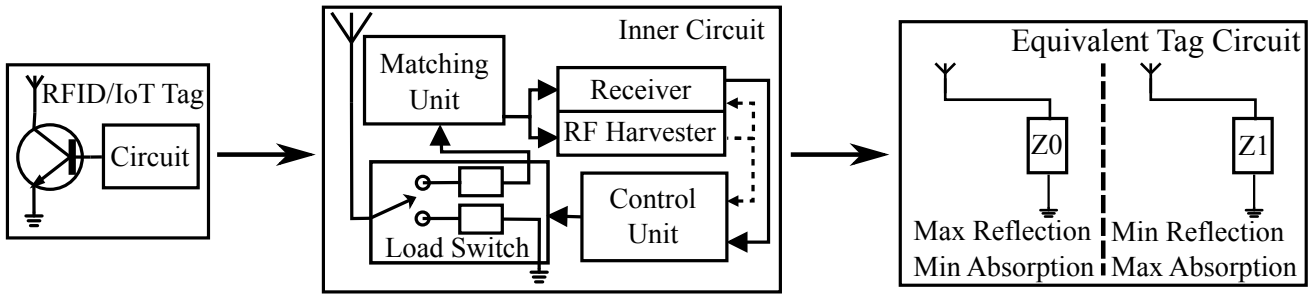

Fig. 1. An RFID/IoT tag terminates its antenna between two loads/states: an "RF energy absorbing" state Z1 (for energy harvesting) or an "RF energy reflecting" state Z0.

to bring the illuminating antenna in the vicinity of the tag. In that way, sufficient energy is provided to the RF energy harvester of the tag, typically designed around diode-based rectifiers; the latter require relatively strong signals to operate, several orders of magnitude stronger than sensitivity values of typical communication receivers [6], [4]. Specifically, work in [10] suggested monostatic front-ends wired to a baseband processor; multiple illuminators connected to a single receiver through networks of multiplexers, expensive RF cables and amplifiers or custom wireless protocols, have been also proposed [28], in order to cover a larger area where tags can be interrogated. Additionally, RFID readers have been installed on top of mobile platforms, e.g., robots and drones, for commercial applications, but also signal relaying [20].

Prior findings on bistatic [7], [15]–[19] or multistatic [3] backscatter radio have shown how such architectures can effectively boost the range of telecommunications. By exploiting the dyadic [11], non-linear nature of wireless propagation, link budget and diversity gain can be achieved [3]. Thus, a multistatic setup has tremendous advantages over its monostatic counterpart, albeit with increased installation cost. Other studies on bistatic backscatter radio include: [30] where the devices backscatter LoRa signals; [8] where IoT nodes backscatter BLE compatible signals; [12] where BLE signals are used as illuminating source, and the tags backscatter Wi-Fi signals. However, none of this prior art touched on Miller line codes and their noncoherent detection.

Study of coherent detection for FM0 and Miller is performed in [29]. Pioneering work in [25], [26] provided approximations of maximum likelihood sequence detection, when dealing with unknown parameters. Generalized likelihood ratio test (GLRT)-optimal noncoherent sequence detection for FM0 was given in [2] with log-linear complexity (with respect to the sequence length); experimental validation for the latter work on industrial Gen2 RFID tags is found in [23]. Work in [9] described an algorithm for GLRT-optimal noncoherent MSK detection, again with log-linear complexity in the sequence length. Work in [21] describes a methodology for low complexity, potentially linear to the sequence length, noncoherent detection. However, the bit error rate (BER) performance is not guaranteed to be near-optimal; BER performance can be enhanced at the cost of complexity, i.e., departing from linear and arriving at approximately quadratic in the sequence length.

This work puts forth a Gen2-compliant, linear complexity noncoherent sequence detection scheme for Miller m, including $m \in \{2, 4, 8\}$. Performance results are provided under Rayleigh and Rician fading, with or without residual carrier frequency offset (CFO). The latter is present in bistatic or multistatic (distributed) setups, where illuminating transmitter and receiver of the tag-backscattered information belong to different terminals. As a result, the compound channel from symbol to symbol is not constant and thus, a coherent detector (that assumes a constant compound channel) would suffer from performance loss. Additionally, this work examines the performance of the proposed detection scheme in both monostatic and multistatic experimental setups that accommodate the industrial Gen2 RFID protocol. To the best of our knowledge, there is no prior art on noncoherent sequence detection algorithms for Miller line codes, let alone being holistically tested under presence of CFO and DC offset. Additionally, this noncoherent algorithm is shown to perform near-optimally, compared to ideal coherent detection (under perfect channel estimation and zero CFO).

Finally, this work provides a software-defined radio (SDR) & Ethernet-based solution for multistatic RFID interrogation. It performs competitively, when compared to other industrial products, in terms of extended coverage and range (tag-receiver distance $\geq$ 30 m), low-cost of infrastructure and installation. Ethernet is nowadays omnipresent in building infrastructure, as opposed to expensive RF cables, while required equipment is based on inexpensive SDRs.

Note that the proposed multistatic architecture is impacted from the timing constraints of the Gen2 protocol more severely than it's monostatic counterpart. This is because baseband packet communication is performed through an Ethernet layer, as well as the fact that the signal processing and control logic is running on software (instead of hardware). As a result, the carrier frequency offset (inherent in multistatic setups) correction and all subsequent processing need to be fast and robust in order to reliably interrogate passive Gen2 RFID tags. This makes the use of a robust, low complexity, noncoherent sequence detection algorithm, a critical detail.

Subfig. 3 (a) visualizes the motivating idea of the multistatic RFID networked reader. It consists of several Tx SDRs and a single Rx SDR, all connected to a computer/PC through Ethernet; the PC creates the baseband samples and submits them to the to Tx SDRs or receives and processes them from the Rx SDR. Note that the Ethernet layer can be replaced with

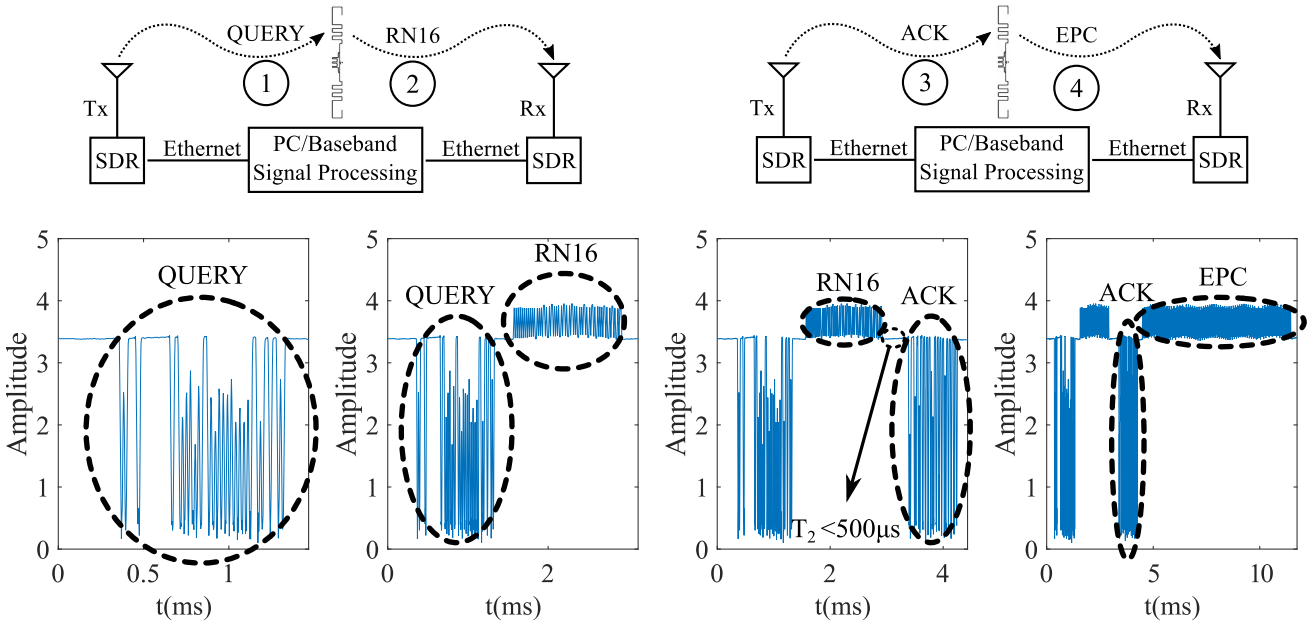

Fig. 2. Gen2 interrogation under distributed, bistatic operation using 2 SDRs (one for illumination and one for reception).

any other sufficiently fast layer, e.g., USB 3. Subfig. 3 (b) visualizes an example of a potentially future application. If we were able to overcome the T_2 limitations through a next generation cellular network, or revise the Gen2 protocol to increase T_2, we could potentially use our cellphones to illuminate RFID tags and pickup the tag-backscattered information by the nearest pico/femto-cell base station. This is the base of the cellular telephone-RFID convergence vision.

Overall, the contributions of this work can be summarized in the following points:

- A novel, Gen2-compliant, noncoherent Miller sequence detection algorithm with linear complexity (in the sequence length). Simulated and experimental results demonstrate the near-optimal flavor of the algorithm and robustness in bistatic setups. The aforementioned noncoherent algorithm is shown to outperform the traditional coherent detection scheme in the presence of residual CFO.
- A multistatic RFID/IoT interrogating architecture, based on commodity, low-cost SDRs, connected over the Ethernet. Experimental results demonstrate increased coverage and range over monostatic setups.

Section II describes the system model (signal model & Miller line code); Section III describes the zero-centered signal model, and offers an important theorem; Section IV & Sec. V describe the coherent and noncoherent sequence detection algorithms, respectively; Section VI offers simulation and experimental results. Finally, work is concluded in Section VII.

NOTATION

Notation: $\mathcal{CN}(\mathbf{m},\mathbf{C})$ denotes the proper complex Gaussian distribution of mean $\mathbf{m}$ and covariance matrix $\mathbf{C}$. The conjugate of a complex number w is denoted as w^H; in the case of a complex vector $\mathbf{z}$, conjugate transpose (hermitian) is denoted also as $\mathbf{z}^H$. The inner product of two complex vectors $\mathbf{u},\mathbf{v}$ is denoted as $\langle \mathbf{u},\mathbf{v}\rangle = \mathbf{u}^H\mathbf{v}$. The real part of a complex number w is given by $\Re\{w\}$. $\|\mathbf{x}\|_2 = \sqrt{\mathbf{x}^H\mathbf{x}}$ denotes the Euclidean norm of complex vector $\mathbf{x}$. $\mathbb{I}(\cdot)$ is an indicator function that returns 1 if its argument is true and 0, otherwise. Finally, $\mathcal{U}(a,b)$ denotes the uniform probability distribution in the range $[a,b]$.

II. SYSTEM MODEL

The bistatic signal model is initially assumed, where transmitter (TX) illuminates a tag, which reflects/scatters back towards a receiver (RX), as shown in Fig. 2. The signal model of the samples received from the software defined radio (SDR) follows [15]:

$$\begin{aligned}\mathrm{y}[k] &= \left(\sqrt{2P_\mathrm{c}}h_\mathrm{CR} + \sqrt{2P_\mathrm{c}}h\,\mathrm{s}\,\mathrm{x}_\mathrm{tag}[k]\right)\mathrm{e}^{-\mathrm{j}(2\pi\Delta f k T_\mathrm{s}+\Delta\phi_\mathrm{R})} \\ &\quad + \mathrm{n}[k] \\ &= \left(m_\mathrm{dc} + m_\mathrm{tag}\mathrm{x}_\mathrm{tag}[k]\right)\mathrm{e}^{-\mathrm{j}(2\pi\Delta f k T_\mathrm{s}+\Delta\phi_\mathrm{R})} + \mathrm{n}[k]\,, \quad (1)\end{aligned}$$

where T_s is the receiver's sampling period, Δf denotes the carrier frequency offset (CFO) and $\Delta\phi_\mathrm{R}$ denotes the carrier phase offset (CPO) between transmitting and receiving SDR; tag's signal $\mathrm{x}_\mathrm{tag}[k] \in \{\Gamma_0,\Gamma_1\}$, where Γ_0,Γ_1 correspond to the reflection coefficients for the reflecting and absorbing states of the tag, respectively; P_c is the transmission (Tx) power of the transmitting SDR and $\mathrm{s} \in (0,1)$ denotes the tag's scattering efficiency; thermal noise of the receiver is modeled by $\mathrm{n}[k] \sim \mathcal{CN}(0,\sigma_\mathrm{n}^2)$, attaining power proportional to the receiving bandwidth of the SDR; different noise samples (i.e., $\mathrm{w}[k],\mathrm{w}[m], k \neq m$) are independent. Rician flat fading is assumed:

$$h_\mathrm{q} \sim \mathcal{CN}\left(\sqrt{\frac{\mathrm{k_q}}{\mathrm{k_q}+1}\sigma_\mathrm{q}^2}, \frac{\sigma_\mathrm{q}^2}{\mathrm{k_q}+1}\right),\ \mathrm{q} \in \{\mathrm{CR},\mathrm{CT},\mathrm{TR}\}\,, \quad (2)$$

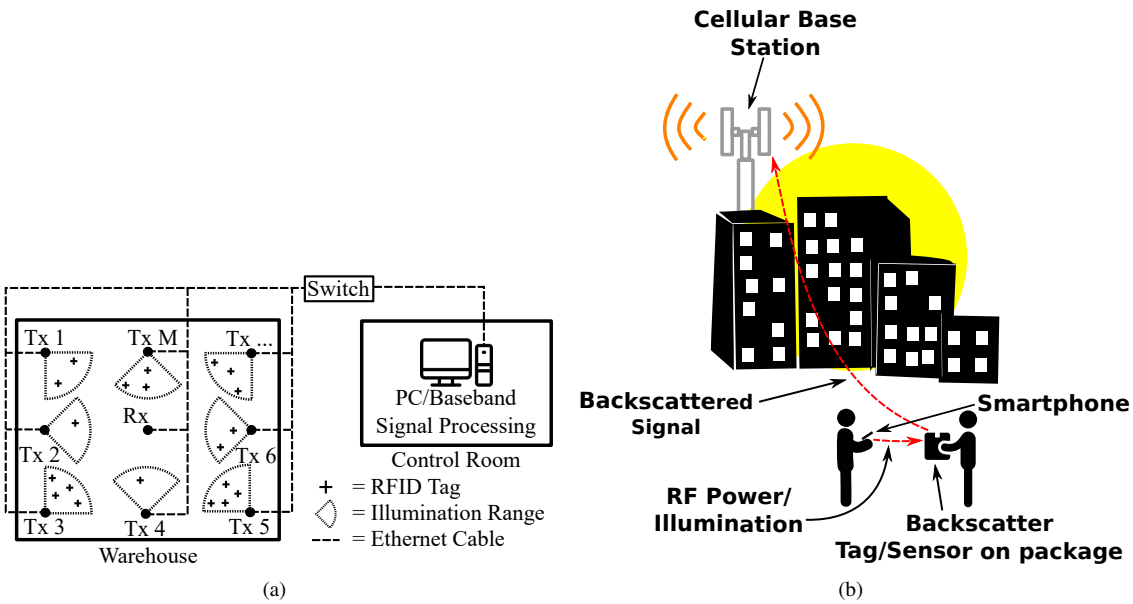

Fig. 3. Convergence Vision: Could existing (e.g., LAN) or future (e.g., cellular) network infrastructure read commercial (Gen2) RFID tags? (a): Deployment of multiple SDR transmitters/illuminators along with a single receiving SDR in a warehouse. Each transmitter covers a specific sector. The system avoids lossy and expensive coaxial extension cables and amplifier units by using conventional SDRs networked through Ethernet. (b): Future vision example. A smartphone illuminates the backscatter tag on a package. The backscattered signal is received by the cellular base station. The base station informs the smartphone user about the tag information through SMS.

where $\mathrm{CR}, \mathrm{CT}, \mathrm{TR}$ denote the carrier/illuminator-to-receiver, carrier-to-tag and tag-to-receiver links, accordingly, and $\sigma_{\mathrm{q}}^2 = \mathbb{E}\left[|h_{\mathrm{q}}|^2\right]$; $\mathrm{k_q}$ corresponds to the power ratio of the direct (line-of-sight) path over the scattered paths. For the special case of $\mathrm{k_q} = 0$, Rayleigh fading is obtained. Complex channel parameter h_{q} is assumed constant for the duration of a backscattered packet and changes independently between successive packets. Furthermore, $h \triangleq h_{\mathrm{CT}} h_{\mathrm{TR}} \in \mathbb{C}$.

It has to be noted that tag's antenna structural mode parameter $A_{\mathrm{s}} \in \mathbb{C}$ can be absorbed in the dc term m_{dc}. Eq. (1) simply states that the received signal is the superposition of the direct signal from carrier illuminator-to-receiver and the signal reflected/backscattered from the tag (after illumination from the transmitter) towards the receiver, taking into account CFO and CPO between transmitter/illuminator and receiver. The illuminating signal contributes a dc term at the receiver, denoted as m_{dc} above.

In the monostatic case, further simplifications are possible; a single device is responsible for both transmission and reception with a common oscillator and thus, it can be assumed that $\Delta f = \Delta\phi_{\mathrm{R}} = 0$, i.e., transmit and receive chains share the same oscillator. Additionally, complex gain parameter h_{CR} denotes the transmit-to-receive chain leakage, while due to antenna proximity, full correlation $h_{\mathrm{CT}} = h_{\mathrm{TR}}$ is assumed [3] and thus, $h = h_{\mathrm{CT}}^2$.

Assuming matched filtering, dc offset removal and symbol-level synchronization, the signal model of Eq. (1) is simplified to the following form [13]:

$$\mathrm{y}\left[i\right] = \tilde{h}\, \mathrm{x_{tag}}[i] + \mathrm{w}\left[i\right], \tag{3}$$

where $\tilde{h} = L\sqrt{2P_{\mathrm{c}}} h\, \mathrm{s}$ and L is a carefully defined over-sampling factor. Specifically, denoting bit duration as T_{b} and defining that each "high" or "low" level of the baseband signal is a part of the bit, i.e., a *chip*, then $L = \frac{T_{\mathrm{b}}}{2mT_{\mathrm{s}}}$ is the number of samples per chip; integer $m \in \{2, 4, 8\}$ depends on the specific Miller line code used, explained in more detail subsequently. For chip index i, it follows that $\mathrm{x_{tag}}[i] \in \{0, 1\}$ and $\mathrm{w}\left[i\right] \sim \mathcal{CN}\left(0, L\sigma_{\mathrm{n}}^2\right)$. Eq. (3) is valid for both monostatic, as well as bistatic systems; in the latter case, perfect CFO and CPO compensation is assumed. In the simulation, as well as experimental results for the bistatic (or multistatic case), such assumption of perfect carrier synchronization will be relaxed.

A. Miller Line Code

Miller line coding offers 4 possible waveforms, two for each bit. The waveforms for information bit-1 do not change the line level at the middle of the bit, whereas the waveforms for bit-0 do. Additionally, the starting line level of each waveform must be opposite than that of the preceding waveform. The exception to that rule is when there is transmission of bit-1 after bit-0; in that case, the line level at the start of both waveforms must be the same.

Fig. 4 demonstrates how each Miller line code encodes its symbols and which transitions are allowed. Notation wise, 1-High and 1-Low refer to symbols of bit-1, when the line begins at high and low level, respectively, while 0-High and 0-Low refer to bit-0, in the same manner. For Miller 2, those four symbols/waveforms are denoted as $\mathbb{S}_2 = \{\mathbf{S}_{21},\ \mathbf{S}_{22},\ \mathbf{S}_{23},\ \mathbf{S}_{24}\}$. Notice that consecutive bits allow for specific waveforms to be used; for example, when bit-1 Low, i.e., $\mathbf{S}_{22}$ is the previous bit, $\mathbf{S}_{23}$ ($\mathbf{S}_{21}$) is the only possible waveform for the next bit when the tag needs to transmit bit-0 (bit-1). Also notice how the line level is the same at the beginning of the last two bits (from bit-0 to bit-1) of Fig. 4. All possible transitions are depicted in Fig. 5. The same rules apply to Miller 4/8. The

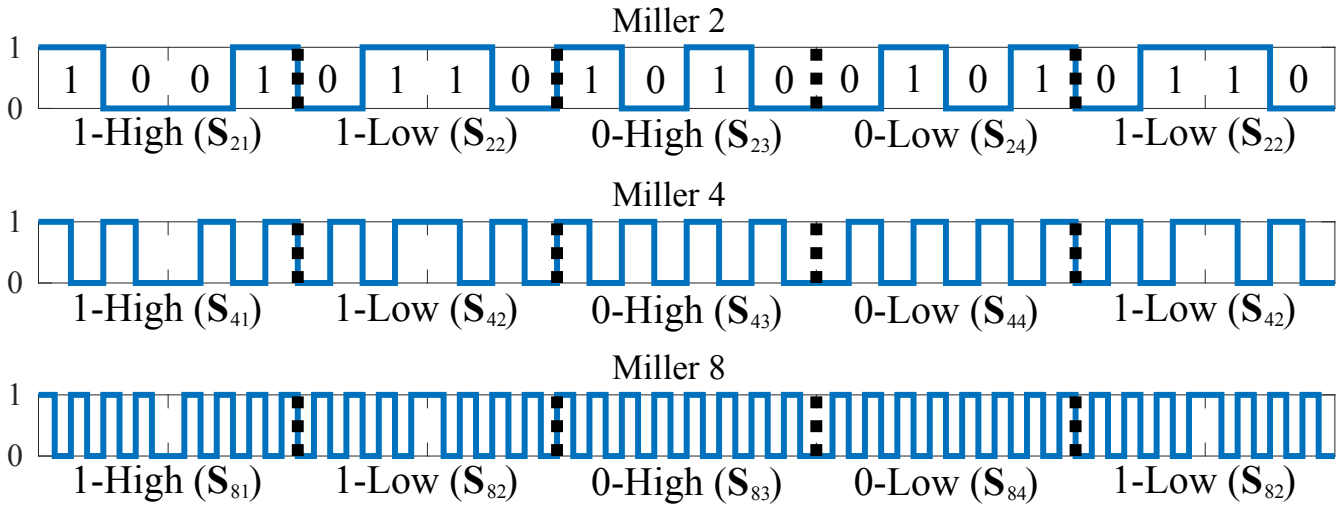

Fig. 4. Miller 2, 4, 8 waveforms example: the black vertical dashes denote the bit boundaries. Miller 4, 8 offers 2, 4 times higher number of transitions per bit, respectively, compared to Miller 2.

only difference of Miller 4 (8) compared to Miller 2 is that there are $2\times$ ($4\times$) additional transitions per bit (Fig. 4). In conjunction with that, changing the Miller line code from 2 to 4 (8) for Gen2 RFID tags, without tinkering with other tag options, results to $2\times$ ($4\times$) bit duration, due to constant chip duration.

III. Zero-Centered vs β-Centered Miller Line Coding

Assuming Miller m, $m \in \{2,\ 4,\ 8\}$ line coding and N tag-reflected bits, Eq. (3) is rewritten as follows:

$$\mathbf{y}_m[n] = \begin{bmatrix} y[4n+0] \\ y[4n+1] \\ \vdots \\ y[4n+2m-1] \end{bmatrix} = \tilde{h}\,\mathbf{x}_m[n] + \mathbf{w}_m[n],\ n = 0, 1, \ldots, N-1, \quad (4)$$

where $\{\mathbf{w}_m[n]\}$ are i.i.d., $\mathbf{w}_m[n] \sim \mathcal{CN}(\mathbf{0}, L\sigma_{\rm n}^2\mathbf{I}_{2m})$ and $\mathbf{x}_m[n]$ is Miller-encoded data vector; the latter can be written compactly (and perhaps elegantly[1]), as follows:

$$\mathbf{x}_m[n] \in \mathbb{S}_m = \{\mathbf{S}_{m1},\ \mathbf{S}_{m2},\ \mathbf{S}_{m3},\ \mathbf{S}_{m4}\}, \quad (5)$$

with set $\mathbb{S}_m$ defined below, for all values of m. Vectors $\mathbf{S}_{m1}$, $\mathbf{S}_{m2}$ correspond to bit-1, while $\mathbf{S}_{m3}$, $\mathbf{S}_{m4}$ correspond to bit-0; there are two vectors per bit, depending on whether the corresponding (line) waveform starts at high or low level.

Specifically, for Miller $m = 2$ waveforms, as shown in Fig. 4 / first row, $\mathbb{S}_2$ is given by:

$$\mathbf{S}_{21} = \begin{bmatrix}1 & 0 & 0 & 1\end{bmatrix}^T,\ \mathbf{S}_{22} = \begin{bmatrix}0 & 1 & 1 & 0\end{bmatrix}^T,$$
$$\mathbf{S}_{23} = \begin{bmatrix}1 & 0 & 1 & 0\end{bmatrix}^T,\ \mathbf{S}_{24} = \begin{bmatrix}0 & 1 & 0 & 1\end{bmatrix}^T,$$

where the first line corresponds to bit-1 and the second line to bit-0. Fig. 4 / first row shows that the line level does not change at the middle of the bit for $\mathbf{S}_{21}$ or $\mathbf{S}_{22}$, as opposed to the case of $\mathbf{S}_{23}$ or $\mathbf{S}_{24}$. Such rules are encoded at the vector definitions above. Moreover, the line changes level at the beginning of each bit, compared to the line level at the beginning of the previous bit; the only exception to this rule is the transition from bit-0 to bit-1. Such rules can only be seen in bit sequences, with an example shown at Fig. 4.

[1]...to the best of our knowledge, such compact representation for Miller has not appeared in the literature before.

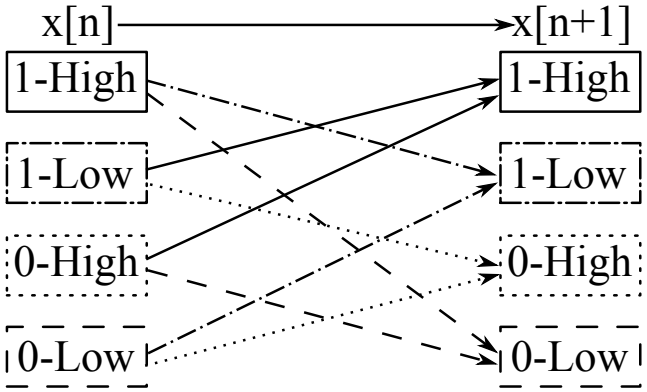

Fig. 5. Allowed transitions in Miller line coding.

Similar reasoning follows for elements of $\mathbb{S}_4$ or $\mathbb{S}_8$, given below (they could be easily checked with the help of Fig. 4):

$$\mathbf{S}_{41} = \begin{bmatrix}\mathbf{S}_{23}^T & \mathbf{S}_{24}^T\end{bmatrix}^T,$$
$$\mathbf{S}_{42} = \begin{bmatrix}\mathbf{S}_{24}^T & \mathbf{S}_{23}^T\end{bmatrix}^T,$$
$$\mathbf{S}_{43} = \begin{bmatrix}\mathbf{S}_{23}^T & \mathbf{S}_{23}^T\end{bmatrix}^T,$$
$$\mathbf{S}_{44} = \begin{bmatrix}\mathbf{S}_{24}^T & \mathbf{S}_{24}^T\end{bmatrix}^T,$$
$$\mathbf{S}_{81} = \begin{bmatrix}\mathbf{S}_{23}^T & \mathbf{S}_{23}^T & \mathbf{S}_{24}^T & \mathbf{S}_{24}^T\end{bmatrix}^T,$$
$$\mathbf{S}_{82} = \begin{bmatrix}\mathbf{S}_{24}^T & \mathbf{S}_{24}^T & \mathbf{S}_{23}^T & \mathbf{S}_{23}^T\end{bmatrix}^T,$$
$$\mathbf{S}_{83} = \begin{bmatrix}\mathbf{S}_{23}^T & \mathbf{S}_{23}^T & \mathbf{S}_{23}^T & \mathbf{S}_{23}^T\end{bmatrix}^T,$$
$$\mathbf{S}_{84} = \begin{bmatrix}\mathbf{S}_{24}^T & \mathbf{S}_{24}^T & \mathbf{S}_{24}^T & \mathbf{S}_{24}^T\end{bmatrix}^T.$$

A. Zero-Centered Miller Coding

Miller $m \in \{2,\ 4,\ 8\}$ symbols of Fig. 4 are centered around $\beta = \frac{1}{2}$. Thus, $\forall i \in \{1,\ 2,\ 3,\ 4\}$, $\forall m \in \{2,\ 4,\ 8\}$, $\mathbf{S}_{mi} \in \mathbb{S}_m$ can be rewritten as follows:

$$\begin{aligned}\mathbf{S}_{mi} = \mathbf{S}_{mi} + (\beta - \beta)\mathbf{1}_{2m} &= (\mathbf{S}_{mi} - \beta\mathbf{1}_{2m}) + \beta\mathbf{1}_{2m} \\ &= \hat{\mathbf{S}}_{mi} + \beta\mathbf{1}_{2m}, \end{aligned} \tag{6}$$

where $\mathbf{1}_{2m}$ denotes a $2m \times 1$ vector with all elements equal to 1 and

$$\hat{\mathbb{S}}_m = \{\hat{\mathbf{S}}_{m1},\ \hat{\mathbf{S}}_{m2},\ \hat{\mathbf{S}}_{m3},\ \hat{\mathbf{S}}_{m4}\}$$

is the set containing the *zero-centered* symbols of Miller m. For illustration purposes, zero-centered Miller $m = 2$ symbols are defined below:

$$\hat{\mathbf{S}}_{21} = \frac{1}{2}\begin{bmatrix}+1 & -1 & -1 & +1\end{bmatrix}^T,\ \hat{\mathbf{S}}_{22} = -\hat{\mathbf{S}}_{21},$$
$$\hat{\mathbf{S}}_{23} = \frac{1}{2}\begin{bmatrix}+1 & -1 & +1 & -1\end{bmatrix}^T,\ \hat{\mathbf{S}}_{24} = -\hat{\mathbf{S}}_{23}.$$

Assuming perfect knowledge of channel parameter $\tilde{h}$, which is not a prerequisite as will be shown in Section V, a zero-centered signal model with Miller m line coding can be derived:

$$\begin{aligned}\hat{\mathbf{y}}_m[n] &\triangleq \mathbf{y}_m[n] - \beta\tilde{h}\mathbf{1}_{2m} \\ &= \tilde{h}\left(\mathbf{x}_m[n] - \beta\mathbf{1}_{2m}\right) + \mathbf{w}_m[n] \\ &\overset{(6)}{=} \tilde{h}\,\hat{\mathbf{x}}_m[n] + \mathbf{w}_m[n],\ n = 0, 1, \ldots, N-1, \end{aligned} \tag{7}$$

where β is a scaling, user-defined system parameter apriori known and $\hat{\mathbf{x}}_m \in \hat{\mathbb{S}}_m$. Consecutively, $\forall i, j \in \{1,\ 2,\ 3,\ 4\}$ and for each $m \in \{2,\ 4,\ 8\}$:

$$\begin{aligned}\left\langle \hat{\mathbf{S}}_{mj},\ \mathbf{S}_{mi} \right\rangle &= \left\langle \hat{\mathbf{S}}_{mj},\ \hat{\mathbf{S}}_{mi} + \beta\mathbf{1}_{2m} \right\rangle \\ &= \left\langle \hat{\mathbf{S}}_{mj},\ \hat{\mathbf{S}}_{mi} \right\rangle + \beta\left\langle \hat{\mathbf{S}}_{mj},\ \mathbf{1}_{2m} \right\rangle \\ &= \left\langle \hat{\mathbf{S}}_{mj},\ \hat{\mathbf{S}}_{mi} \right\rangle, \end{aligned} \tag{8}$$

since $\left\langle \hat{\mathbf{S}}_{mj},\ \mathbf{1}_{2m} \right\rangle = 0$, due to equal number of $\{+\frac{1}{2}, -\frac{1}{2}\}$ elements in $\hat{\mathbf{S}}_{mj}$.

Having derived Eq. (8), this Section concludes with the following useful result:

$$\begin{aligned}\left\langle \hat{\mathbf{S}}_{mj},\ \hat{\mathbf{y}}_m[n] \right\rangle &= \left\langle \hat{\mathbf{S}}_{mj},\ \tilde{h}\,\hat{\mathbf{x}}_m[n] + \mathbf{w}_m[n] \right\rangle \\ &= \tilde{h}\left\langle \hat{\mathbf{S}}_{mj},\ \hat{\mathbf{x}}_m[n] \right\rangle + \left\langle \hat{\mathbf{S}}_{mj}, \mathbf{w}_m[n] \right\rangle \\ &\overset{(8)}{=} \tilde{h}\left\langle \hat{\mathbf{S}}_{mj},\ \mathbf{x}_m[n] \right\rangle + \left\langle \hat{\mathbf{S}}_{mj}, \mathbf{w}_m[n] \right\rangle \\ &= \left\langle \hat{\mathbf{S}}_{mj},\ \tilde{h}\mathbf{x}_m[n] + \mathbf{w}_m[n] \right\rangle \\ &= \left\langle \hat{\mathbf{S}}_{mj},\ \mathbf{y}_m[n] \right\rangle. \end{aligned} \tag{9}$$

This finding is formally stated below:

Theorem 1: Let $\hat{\mathbf{x}}_m[n] \in \hat{\mathbb{S}}_m,\ m \in \{2,\ 4,\ 8\}$, $\mathbf{y}_m[n]$ any β-centered Miller m signal model and $\hat{\mathbf{y}}_m[n]$ its equivalent zero-centered signal model. The following holds:

$$\langle \hat{\mathbf{x}}_m[n],\ \hat{\mathbf{y}}_m[n] \rangle = \langle \hat{\mathbf{x}}_m[n],\ \mathbf{y}_m[n] \rangle. \tag{10}$$

The above Theorem essentially suggests that perfect DC cancellation is not needed for inner products in the form of Eq. (10). In addition to that, further backscattered-waveform centering, which requires estimation/knowledge of channel $\tilde{h}$, is not required. However, the reason why this theorem is so important is because inner products in the form of Eq. (10) are used as part of the metrics for the detection algorithms presented in Sec. IV & Sec. V. Thus, the proposed linear non-coherent sequence detection algorithm is truly noncoherent.

IV. $\mathcal{O}(N)$ Complexity Optimal Coherent Sequence Detection

The coherent detection is briefly discussed in order to be used as a lower bound for the bit error rate (BER) performance of the proposed noncoherent sequence detection scheme.

As examined above in Fig. 4 and Fig. 5, only specific transitions are allowed. Miller line coding induces memory on the backscattered symbols and thus, BER-optimal coherent detection requires sequence detection.

Since the conditional probability density is defined given knowledge of channel $\tilde{h}$, then the system model of Eq. (7) can be used instead of that in Eq. (4). The conditional probability density $f(\cdot|\cdot)$ is given by:

$$f\left(\hat{\mathbf{y}}_m[n]\middle|\hat{\mathbf{x}}_m[n],\ \tilde{h}\right) \sim \mathcal{CN}(\tilde{h}\,\hat{\mathbf{x}}_m[n], L\sigma_{\mathrm{n}}^2\mathbf{I}_{2m}) \tag{11}$$

$$\propto \exp\left(-\frac{1}{L\sigma_{\mathrm{n}}^2}\left\|\hat{\mathbf{y}}_m[n] - \tilde{h}\,\hat{\mathbf{x}}_m[n]\right\|_2^2\right), \tag{12}$$

and thus, the conditional probability density for the whole sequence is given by:

$$f\left(\hat{\mathbf{y}}_m\middle|\hat{\mathbf{x}}_m,\ \tilde{h}\right) = \prod_{n=0}^{N-1} f\left(\hat{\mathbf{y}}_m[n]\middle|\hat{\mathbf{x}}_m[n],\ \tilde{h}\right), \tag{13}$$

where $\hat{\mathbf{y}}_m,\ \hat{\mathbf{x}}_m$ are the sets containing all the $\hat{\mathbf{y}}_m[n],\ \hat{\mathbf{x}}_m[n]$, respectively. It is crucial to note that $\hat{\mathbf{x}}_m \in \mathcal{X}_m$, where $\mathcal{X}_m$ is the set of all valid N-bit Miller-encoded sequences. Hence, the BER-optimal sequence can be found solving the following maximum likelihood (ML) problem:

$$\begin{aligned}\hat{\mathbf{x}}_m^{\mathrm{ML}} &= \underset{\hat{\mathbf{x}}_m \in \mathcal{X}_m}{\operatorname{argmax}} \prod_{n=0}^{N-1} f\left(\hat{\mathbf{y}}_m[n]\middle|\hat{\mathbf{x}}_m[n],\ \tilde{h}\right) \\ &= \underset{\hat{\mathbf{x}}_m \in \mathcal{X}_m}{\operatorname{argmax}} \prod_{n=0}^{N-1} \exp\left(-\frac{1}{L\sigma_{\mathrm{n}}^2}\left\|\hat{\mathbf{y}}_m[n] - \tilde{h}\,\hat{\mathbf{x}}_m[n]\right\|_2^2\right) \\ &= \underset{\hat{\mathbf{x}}_m \in \mathcal{X}_m}{\operatorname{argmin}} \sum_{n=0}^{N-1} \left\|\hat{\mathbf{y}}_m[n] - \tilde{h}\,\hat{\mathbf{x}}_m[n]\right\|_2^2 \\ &= \underset{\hat{\mathbf{x}}_m \in \mathcal{X}_m}{\operatorname{argmin}} \sum_{n=0}^{N-1} \Bigg(\|\hat{\mathbf{y}}_m[n]\|_2^2 + \left\|\tilde{h}\,\hat{\mathbf{x}}_m[n]\right\|_2^2 \\ &\qquad -2\Re\left\{\left\langle \tilde{h}\,\hat{\mathbf{x}}_m[n], \hat{\mathbf{y}}_m[n] \right\rangle\right\}\Bigg) \\ &\overset{(a)}{=} \underset{\hat{\mathbf{x}}_m \in \mathcal{X}_m}{\operatorname{argmax}} \sum_{n=0}^{N-1} \Re\left\{\tilde{h}^H \langle \hat{\mathbf{x}}_m[n], \hat{\mathbf{y}}_m[n] \rangle\right\} \\ &\overset{\text{Th. 1}}{=} \underset{\hat{\mathbf{x}}_m \in \mathcal{X}_m}{\operatorname{argmax}} \sum_{n=0}^{N-1} \Re\left\{\tilde{h}^H \langle \hat{\mathbf{x}}_m[n], \mathbf{y}_m[n] \rangle\right\}, \end{aligned} \tag{14}$$

where in (a) the fact that $\|\hat{\mathbf{x}}_m[n]\|_2^2 = \text{constant}, \forall\ \hat{\mathbf{x}}_m[n] \in \hat{\mathbb{S}}_m, \forall$ Miller m line code, was exploited.

This maximization problem can be solved with the Viterbi algorithm (VA) with linear (to the bit sequence length) complexity, on a Trellis diagram based on Fig. 5 and weights $W_{n,i} = \Re\left\{\tilde{h}^H \langle \hat{\mathbf{x}}_m[n], \mathbf{y}_m[n]\rangle\right\}$, where n denotes the nth bit and i denotes the Trellis diagram state, i.e., $\hat{\mathbf{x}}_m[n] = \hat{\mathbf{S}}_{mi}$.

It is further noted that channel $\tilde{h}$ can be readily estimated using the preamble bits of Gen2 (or the extra pilot bits), e.g., with a least squares technique. Application of Th. 1 allows the detector to transition from the zero-centered signal model of Eq. (7) back to the β-centered signal model of Eq. (4).

V. $\mathcal{O}(N)$ Complexity Noncoherent Sequence Detection

Considering channel parameter $\hat{h}$ an unknown constant, the generalized likelihood ratio test (GLRT) sequence detection rule is first derived; its form will guide the derivation of the proposed noncoherent algorithm of this work.

The maximum likelihood (ML) estimate of $\tilde{h}$ follows:

$$\begin{aligned}
\hat{h} &= \underset{\tilde{h}\in\mathbb{C}}{\operatorname{argmax}}\, f\left(\hat{\mathbf{y}}_m \middle| \hat{\mathbf{x}}_m,\ \tilde{h}\right) \\
&= \underset{\tilde{h}\in\mathbb{C}}{\operatorname{argmin}} \sum_{n=0}^{N-1} \left\|\hat{\mathbf{y}}_m[n] - \tilde{h}\hat{\mathbf{x}}_m[n]\right\|_2^2 \\
&= \underset{\tilde{h}\in\mathbb{C}}{\operatorname{argmin}} \sum_{n=0}^{N-1} \Big(\|\hat{\mathbf{y}}_m[n]\|_2^2 + \tilde{h}^H\tilde{h}\,\|\hat{\mathbf{x}}_m[n]\|_2^2 \\
&\qquad - \tilde{h}^H \langle \hat{\mathbf{x}}_m[n],\ \hat{\mathbf{y}}_m[n]\rangle - \tilde{h}\,\langle \hat{\mathbf{y}}_m[n],\ \hat{\mathbf{x}}_m[n]\rangle \Big) \\
&= \underset{\tilde{h}\in\mathbb{C}}{\operatorname{argmin}}\, G(\tilde{h}, \hat{\mathbf{x}}_m, \hat{\mathbf{y}}_m). \qquad (15)
\end{aligned}$$

Thus, the estimate follows:

$$\begin{aligned}
&\frac{\partial}{\partial\tilde{h}} G(\tilde{h}, \hat{\mathbf{x}}_m, \hat{\mathbf{y}}_m)\bigg|_{\tilde{h}=\hat{h}} = 0 \Leftrightarrow \\
&\sum_{n=0}^{N-1} \hat{h}^H \|\hat{\mathbf{x}}_m[n]\|_2^2 = \sum_{n=0}^{N-1} \langle \hat{\mathbf{y}}_m[n],\ \hat{\mathbf{x}}_m[n]\rangle \Leftrightarrow \\
&\hat{h} = \frac{\sum_{n=0}^{N-1} \langle \hat{\mathbf{x}}_m[n],\ \hat{\mathbf{y}}_m[n]\rangle}{\sum_{n=0}^{N-1} \|\hat{\mathbf{x}}_m[n]\|_2^2}. \qquad (16)
\end{aligned}$$

That channel estimate can now be used to detect the GLRT-optimal sequence, as follows:

$$\begin{aligned}
\hat{\mathbf{x}}_m^{\text{GLRT}} &= \underset{\hat{\mathbf{x}}_m\in\mathcal{X}_m}{\operatorname{argmax}} \prod_{n=0}^{N-1} f\left(\hat{\mathbf{y}}_m[n] \middle| \hat{\mathbf{x}}_m[n],\ \hat{h}\right) \\
&= \underset{\hat{\mathbf{x}}_m\in\mathcal{X}_m}{\operatorname{argmin}} \sum_{n=0}^{N-1} \left\|\hat{\mathbf{y}}_m[n] - \hat{h}\,\hat{\mathbf{x}}_m[n]\right\|_2^2 \\
&= \underset{\hat{\mathbf{x}}_m\in\mathcal{X}_m}{\operatorname{argmin}} \sum_{n=0}^{N-1} \left(\left\|\hat{h}\,\hat{\mathbf{x}}_m[n]\right\|_2^2 - 2\Re\left\{\hat{h}^H \langle \hat{\mathbf{x}}_m[n], \hat{\mathbf{y}}_m[n]\rangle\right\}\right) \\
&= \underset{\hat{\mathbf{x}}_m\in\mathcal{X}_m}{\operatorname{argmin}} \left(\left\|\hat{h}\right\|_2^2 \sum_{n=0}^{N-1} \|\hat{\mathbf{x}}_m[n]\|_2^2 \right. \\
&\qquad \left. -2\sum_{n=0}^{N-1} \Re\left\{\hat{h}^H \langle \hat{\mathbf{x}}_m[n], \hat{\mathbf{y}}_m[n]\rangle\right\}\right) \\
&\overset{(*)}{=} \underset{\hat{\mathbf{x}}_m\in\mathcal{X}_m}{\operatorname{argmin}} \left(\frac{\left\|\sum_{n=0}^{N-1} \langle \hat{\mathbf{x}}_m[n],\ \hat{\mathbf{y}}_m[n]\rangle\right\|_2^2}{\sum_{n=0}^{N-1} \|\hat{\mathbf{x}}_m[n]\|_2^2} \right. \\
&\qquad \left. -2\frac{\left\|\sum_{n=0}^{N-1} \langle \hat{\mathbf{x}}_m[n],\ \hat{\mathbf{y}}_m[n]\rangle\right\|_2^2}{\sum_{n=0}^{N-1} \|\hat{\mathbf{x}}_m[n]\|_2^2}\right) \\
&= \underset{\hat{\mathbf{x}}_m\in\mathcal{X}_m}{\operatorname{argmax}} \left\|\sum_{n=0}^{N-1} \langle \hat{\mathbf{x}}_m[n],\ \hat{\mathbf{y}}_m[n]\rangle\right\|_2^2 \\
&\overset{\text{Th. 1}}{=} \underset{\hat{\mathbf{x}}_m\in\mathcal{X}_m}{\operatorname{argmax}} \left\|\sum_{n=0}^{N-1} \langle \hat{\mathbf{x}}_m[n],\ \mathbf{y}_m[n]\rangle\right\|_2^2, \qquad (17)
\end{aligned}$$

where the identity $\Re\{\|z\|_2^2\} \equiv \|z\|_2^2 = z^H z$ was used in $(*)$. Th. 1 allows the jump between system models (from zero-centered to β-centered). Especially for this noncoherent detector, such transition is extremely important to make the detector as noncoherent as possible. Solving the above naively, through exhaustive search among all possible N-bit sequences, entails exponential complexity of 2^N. However, quadratic complexity with N^2 can be achieved by a modification of [31]. Given that Gen2 EPC identification information is 96-bit long (the payload is $N = 128$-bit long), quadratic complexity detection may be prohibitive for real time applications, especially under the stringent timing constraints of the Gen2 protocol. Below, an algorithm is offered with linear in N complexity. Note that the following algorithm *does not* solve the aforementioned GLRT detection problem. Instead, it approximates the GLRT-optimal cumulative complex weight that maximizes the Euclidean norm of Eq. (17). Thus, it is sub-optimal GLRT-wise; however, it attains low complexity and as it will be shown in the numerical results, surprisingly near-optimal performance, even when compared to ideal coherent sequence detection.

A. Algorithm

The main principle of the proposed algorithm is a simple modification in the VA. Similarly to the coherent scheme, a Trellis diagram (see Fig. 5) is used with complex weights given by the inner product $W_{n,i} = \langle \hat{\mathbf{x}}_m[n],\ \mathbf{y}_m[n]\rangle$, where n denotes the nth bit and i denotes the state of the Trellis diagram, i.e., $\hat{\mathbf{x}}_m[n] = \hat{\mathbf{S}}_{mi}$. The plot twist comes from the fact that the weights are complex (instead of real), and the path comparison is performed upon the weights' absolute values. This means that for every node of the Trellis diagram we add the incoming cumulative complex weights to the nodes inner product and compare the absolute values of the sums, keeping the largest (due to max absolute operator in Eq. (17)). Then, the complex weight of the surviving path is propagated to the

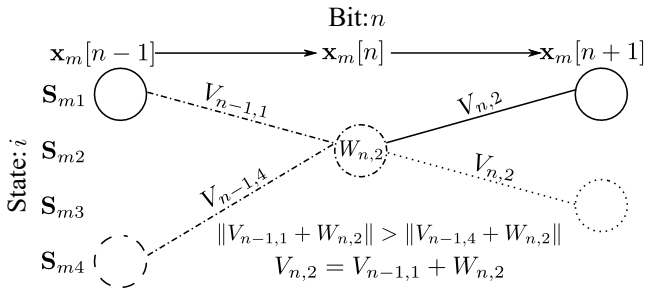

Fig. 6. Example of suggested VA modification, on said Trellis diagram: $W_{n,i}$ denotes the complex weight of the n-th bit to be $\hat{\mathbf{x}}_m[n] = \hat{\mathbf{S}}_{mi}$. $V_{n,i}$ denotes the complex cumulative weight of the surviving path that the n-th bit at the i-th state propagates forward. Note how the absolute values of the metrics are compared; however, the complex value is propagated to the next bit.

next node, instead of the path metric (the absolute value of the complex sum). Such modified operation is depicted in Fig. 6.

The proposed algorithm in tabulated form is given below; notation wise, elements $w[i][n]$ are complex inner product weights of each candidate symbol $\hat{\mathbf{S}}_{mi}$ for the nth bit. The cumulative complex weight of the best path from the 1st bit to the ith candidate symbol of the nth bit is stored in $v[i][n]$. Elements in $p[i][n]$ are the surviving paths that lead to the ith candidate symbol of the nth bit. Also, $\mathbb{P}(n,i)$ is the set of symbols that allow the transition to the ith candidate symbol of the nth bit. Note that this set can be found by looking at the Fig. 5 and taking into account the fact that until the 4th bit, the Trellis graph is not balanced (because only 1-High and 0-High are allowed as first transmitted symbols).

Again, note how Th. 1 allows any β-centered signal model to be used as input to this algorithm, using the vectors in $\hat{\mathbb{S}}_m$ without any knowledge or estimation of h. The algorithm terminates in one pass of the VA, from the first to the last (Nth) bit, and thus, the complexity is linear in N.

Algorithm 1: Linear Noncoherent Miller 2/4/8 Sequence Detection

Input: m, $\mathbf{y}_m$
Output: X_{bits}

Initialize $p[4][N-1]$, $w[4][N]$, $v[4][N]$ to zeros
$w[1][1],\ v[1][1] = \left\langle \hat{\mathbf{S}}_{m1},\ \mathbf{y}_m[1] \right\rangle$
$w[3][1],\ v[3][1] = \left\langle \hat{\mathbf{S}}_{m3},\ \mathbf{y}_m[1] \right\rangle$
for $n = 2:1:N$ **do**
  for $i = 1:1:4$ **do**
    $w[i][n] = \left\langle \hat{\mathbf{S}}_{mi},\ \mathbf{y}_m[n] \right\rangle$
    $j^* = \underset{j \in \mathbb{P}(n,i)}{\text{argmax}} \|v[j][n-1] + w[i][n]\|_2$
    $p[i][n-1] = j^*$
    $v[i][n] = v[j^*][n-1] + w[i][n]$
$j^* = \underset{j \in \{1,2,3,4\}}{\text{argmax}} \|v[j][N]\|_2$
$X_{\text{bits}}[N] = \mathbb{I}(j^* \leq 2)$
for $n = N-1:-1:1$ **do**
  $j^* = p[j^*][n]$
  $X_{\text{bits}}[n] = \mathbb{I}(j^* \leq 2)$
return X_{bits}

VI. Numerical Results

A. Real Time CFO Estimation/Housekeeping

Carrier frequency offset compensation poses the greatest challenge as far as implementing multistatic RFID readers is concerned. As already mentioned in Sec. I, the stringent timing constraint of T_2 between RN16 and ACK must be satisfied, otherwise the protocol times out. In other words, all signal processing and housekeeping task (e.g., CFO & DC compensation) must be performed in a timely manner. As a result, a digital phase locked loop (PLL) was used to compensate the CFO, due to its real-time character. Although a high-resolution periodogram-based technique on large blocks of samples could outperform the PLL solution in terms of CFO compensation, such technique was computationally expensive (too slow) for the purposes of this work, and thus, not suitable.

In the context of simulating and testing the proposed multistatic system, a PLL was developed according to the design in [27, App. C]. A second order loop filter was developed, through experimental observations of the CFO between Tx and Rx SDRs, thus, the PLL was fine-tuned to this specific application. It is noted that, for the simulation part, the PLL CFO tracking was active throughout the time intervals were only the continuous wave (CW) signal from the TX SDR was present, i.e., between QUERY/ACK and RN16/EPC. This was done due to the fact that the PLL was not optimized to track CFO when information was superimposed on top of the CW. Thus, CFO was estimated by solving a least squares-based [14], best linear fit problem, during the CW and then, the estimate was used to compensate the remaining samples that "carry" the tag's information.

Fig. 7 illustrates the cumulative density function (CDF) of the residual CFO, as a function of carrier-to-noise ratio (CNR). This CDF was produced with 10^5 Monte Carlo experiments with initial CFO following a uniform distribution,

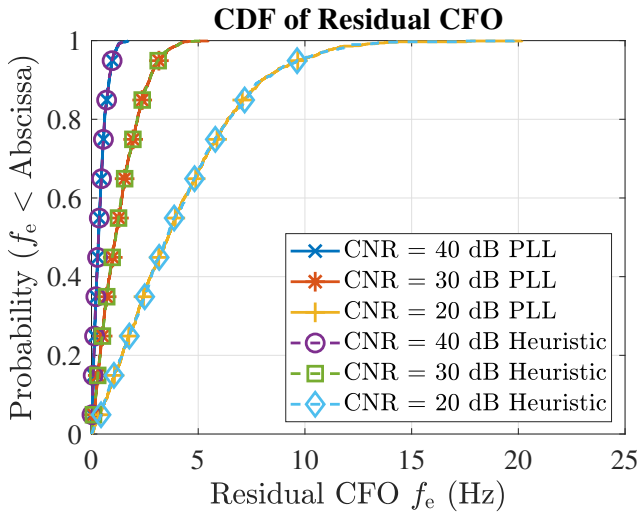

Fig. 7. CDF of the remaining CFO for the two tested CFO compensation methods, PLL and Heuristic.

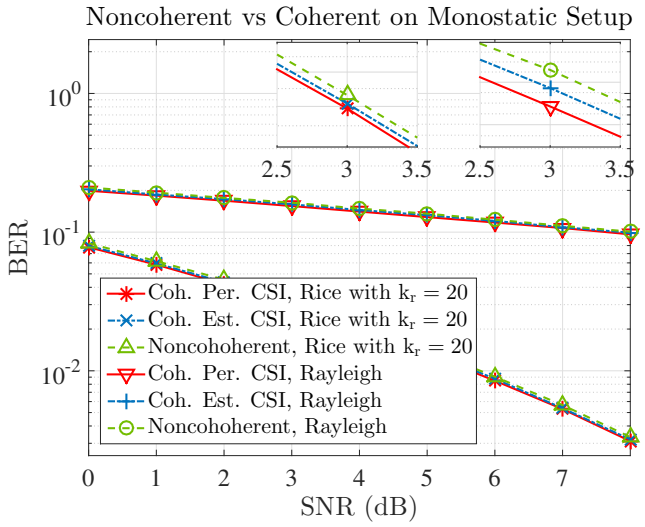

Fig. 8. BER performance of the monostatic model with perfect CFO and DC knowledge. Performance gaps between coherent (assuming either perfect (Prf.Ch) or estimated channel (Est.)) and proposed noncoherent sequence detection are demonstrated under Rayleigh and Rician fading conditions. $N = 128$ for all cases.

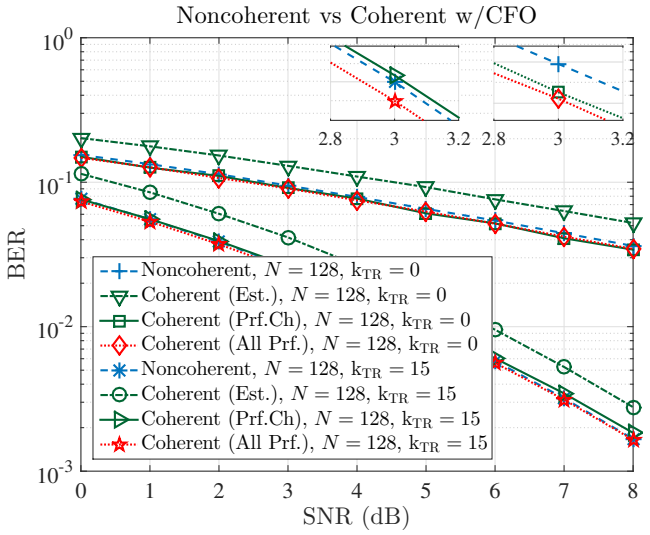

Fig. 9. BER performance of the bistatic model with CFO compensation (using PLL) and dc offset correction. Performance gaps between coherent (assuming either perfect (Prf.Ch) or estimated channel (Est.)) and noncoherent sequence detection are demonstrated under Rayleigh and Rician fading conditions ($\mathrm{k_{CR}} = \mathrm{k_{CT}} = 20$). The case of perfect CFO correction and DC removal is also offered, as baseline (All Prf.).

$\mathcal{U}(-10^5, +10^5)$ Hz. The heuristic method in Fig. 7 is simply a maximum likelihood (ML) phase estimator, $\arctan\left(\frac{\Im\{\mathbf{z}\}}{\Re\{\mathbf{z}\}}\right)$, coupled with a linear fit scheme to estimate the slope of the line (which is the CFO). However, even though they perform similarly in terms of residual CFO,[2] the PLL was chosen as the preferred method due to its real time character.

The aforementioned PLL was also implemented in C++ as an external block for GNURadio, for experimental testing. Even though the results were acceptable, the *"PLL carrier tracking"* GNURadio block was used instead, allowing for easily reproducible results. The PLL block was connected after the *source* (receiving SDR) and before the matched filter blocks and was active throughout the whole interrogation process. The parameters used for that block are: $\frac{10^5\pi}{R}$ (loop bandwidth), $\frac{4\cdot 10^4\pi}{R}$ (max frequency), $\frac{-4\cdot 10^4\pi}{R}$ (min frequency), where $R = 2\cdot 10^6$ denotes the analog-to-digital sampling rate.

Explicit CPO compensation is not required, as it's a constant phase that can be absorbed in the channel parameter. Symbol level synchronization has already been covered in [13], [32], and it's performed with the same manner in this work. Specifically, synchronization is performed by maximizing the a correlation metric using the built-in 10-bit preamble sequence of Gen2 (for Miller line codes). However, energy-based synchronization on the whole package can be performed instead, in order to drop dependencies from the preamble bits.

Channel estimation is also described in prior art, and it's performed (both in simulated and experimental results) with a least squares technique on the the 10-bit preamble sequence of Gen2, similarly to Eq. (16), but using β-centered symbols instead. Note that an optional 12-bit pilot sequence can be activated, but it's not used in this work.

[2]The PLL can be fine-tuned even more, thus potentially achieving better results.

B. Simulation

In order to verify the feasibility of the proposed concept, simulations were performed based on the system model and the detection schemes presented in Sec. IV and Sec. V, respectively. Two cases were considered. The first case studied the performance gap of coherent versus noncoherent detection scheme, assuming perfect CFO compensation and DC offset removal; such case corresponds to the monostatic setup, where CFO is zero. In the second case, both (imperfect) CFO and DC offset correction were considered; that is the case for distributed TX and RX (bistatic or multistatic). Bit error rate (BER) was examined, subject to both Rayleigh and Rician fading, with the latter employing $\mathrm{k_{CT}} = \mathrm{k_{CR}} = 20$ and $\mathrm{k_{TR}} = 15$ for the bistatic setup and $\mathrm{k_r} = \mathrm{k_{CT}} = 20$ for the monostatic. SNR definition follows:

$$\mathrm{SNR} = \frac{2P_{\mathrm{c}}\, L\, \mathrm{s}^2\, \mathbb{E}\left[|\mathrm{x_{tag}}|^2\right]\, \sigma^2_{\mathrm{CT}}\, \sigma^2_{\mathrm{TR}}}{\sigma^2_{\mathrm{n}}}. \tag{18}$$

Without loss of generality, it was assumed that $P_{\mathrm{c}} = 0.50$ W and $\sigma^2_{\mathrm{CT}} = \sigma^2_{\mathrm{TR}} = 1$, while $\mathrm{x_{tag}}[n] \in \{0, 1\}$ was considered. For each SNR value, 10^5 Monte Carlo experiments were performed. Based on Eq. (1), it was further assumed that $m_{\mathrm{dc}} = h_{\mathrm{CR}}|\lambda_{\mathrm{c}}|$, where $\lambda_{\mathrm{c}} \in \mathbb{C}$ a constant related to transmission power and tag-related parameters (e.g., tag structural mode). Carrier-to-noise ratio (CNR) was defined as:

$$\mathrm{CNR} = \frac{\mathbb{E}\left[|m_{\mathrm{dc}}|^2\right]}{\sigma^2_{\mathrm{n}}} = \frac{|\lambda_{\mathrm{c}}|^2\, \sigma^2_{\mathrm{CR}}}{\sigma^2_{\mathrm{n}}}. \tag{19}$$

Thus, for $\sigma^2_{\mathrm{CR}} = 1$, $m_{\mathrm{dc}} = h_{\mathrm{CR}}\sqrt{\mathrm{CNR}\cdot\sigma^2_{\mathrm{n}}}$. Unless otherwise stated, CNR $= 30$ dB. A sequence length of $N = 128$ bits was considered.

Fig. 8 examines the performance of the proposed detectors in a monostatic setup, with perfect CFO and DC compensation. Under Rayleigh fading, it can be observed that the

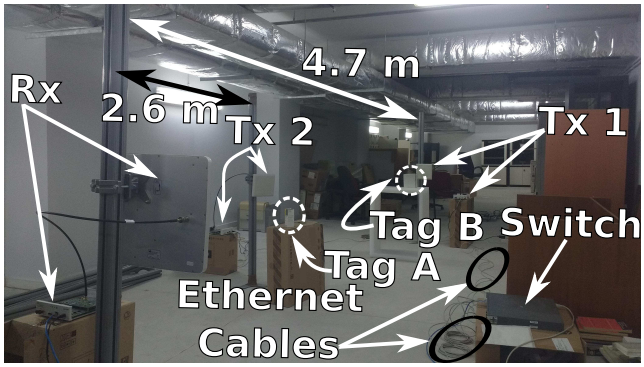

Fig. 10. Multistatic setup utilizing two USRPs as carrier sources/illuminators at 15 dBm and a RTL-SDR (or a USRP) as a receiver. The setup allows for increased coverage with distributed SDR illuminators, operating in a time-division manner and networked over Ethernet.

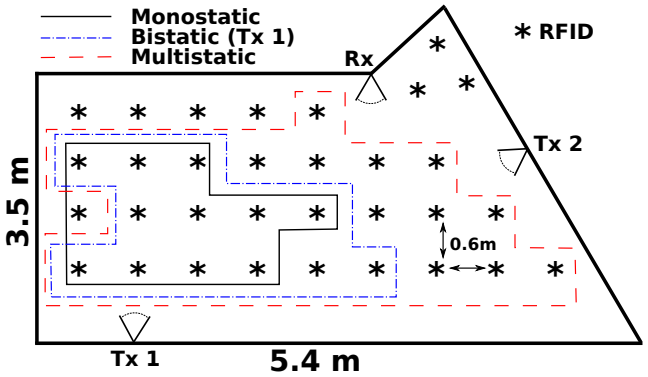

Fig. 11. Area coverage under monostatic, bistatic and multistatic setups. A tag was placed in each of the locations denoted by $*$ and the ability of the reader to interrogate the tag was recorded. Deployment of multiple (dislocated from the receiver) emitters increased coverage; a tag will be more likely to be powered and successfully interrogated if it is in the vicinity of an emitter.

proposed noncoherent scheme performs ≈ 0.50 dB worse than the (ideal) coherent with perfect knowledge of the channel, while the coherent method with estimated channel performs ≈ 0.25 dB worse. Under Rician fading, the performance gap is reduced to ≈ 0.2 and ≈ 0.05 dB for the noncoherent and estimated coherent scheme, respectively.

Fig. 9 examines the performance of the proposed detectors under a detailed bistatic model (Eq. (1), with $L = 125$), including both realistic CFO compensation and DC offset correction. CFO compensation is performed using the PLL, while DC offset is estimated using a sample mean over a specific time interval and is subsequently subtracted from the respective samples. For the coherent cases, channel estimation (where applicable) is performed with the least squares method, utilizing a known training sequence. The first point worth of attention is that under coherent detection, when channel estimate is used, there is a significant performance degradation, even when compared with noncoherent detection. Under Rayleigh (Rician) fading, the gap is ≈ 1.5 dB (≈ 1.2 dB) of coherent detection with estimated channel, compared to all perfect coherent detection.

This finding can be explained by the fact that, due to residual CFO, the phases between successive samples do not remain constant, and thus, channel estimation, which assumes that the parameter to be estimated does not vary for the duration of the training sequence, will not be robust. Furthermore, with residual CFO, the block-constant flat fading assumption does not offer a constant, unknown complex parameter, multiplied by each symbol; instead, each symbol is also multiplied by a time-varying, residual CFO-dependent factor. The above conclusions are further supported by the fact that when the channel parameter is perfectly known, the gap between coherent with perfect CSI vs all perfect coherent reduces to ≈ 0.2 dB for Rayleigh, while for Rician fading, it is observed that noncoherent detector performs slightly better than the coherent employing full channel knowledge (but with residual CFO). Intuitively, this can be explained by the fact that the residual CFO interferes with the deterministic component of the Rice channel (non-zero mean value), and thus the statistics change. Instead, in the case of Rayleigh fading, where there is no deterministic component (zero mean value), the impact of the residual CFO becomes weaker. In the same plot, baseline performance under coherent detection is depicted assuming perfect channel knowledge, CFO compensation and DC removal.

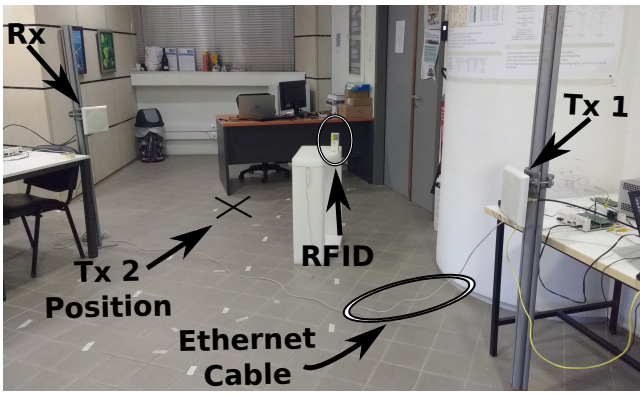

Fig. 12. Experimental setup for one of the instances of Fig. 11. Note that in the monostatic case, the interrogation is carried out only through the "Tx 1" antenna, while in bistatic (and multistatic) case, we take advantage of the extra Rx antenna (and "Tx 2" antenna). This setup also provides a concrete example of the idea demonstrated in Fig. 3 (a).

The above clearly show that the proposed linear complexity noncoherent Miller sequence detection tested in this work, is not only a solid and valid approach, but also advantageous over coherent detection, in the presence of residual CFO (omnipresent in bistatic/multistatic setups) and limited number of preamble bits for channel estimation. Future versions of (multistatic) Gen2 could omit such preamble bits, improving efficiency of communication.

C. Experimentation

The experimental testbed is based upon previous software stack found in [13] and [5], which is augmented with the aforementioned detection algorithms, as well as multistatic capabilities.

First, as a baseline experiment, a monostatic setup is tested, using an Impinj Speedway R1000 RFID reader with a single antenna, in order to verify the maximum reading range with

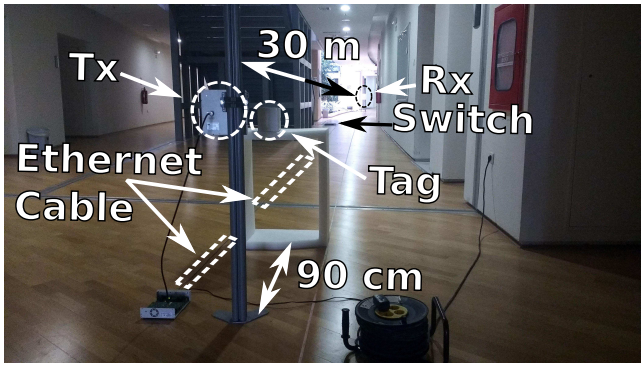

Fig. 13. Bistatic setup utilizing a single USRP as illuminating source (15 dBm) and a USRP or RTL-SDR as receiver. Carrier-to-receiver ranges of at least 30 meters were observed, for a carrier-to-tag distance of 90 cm.

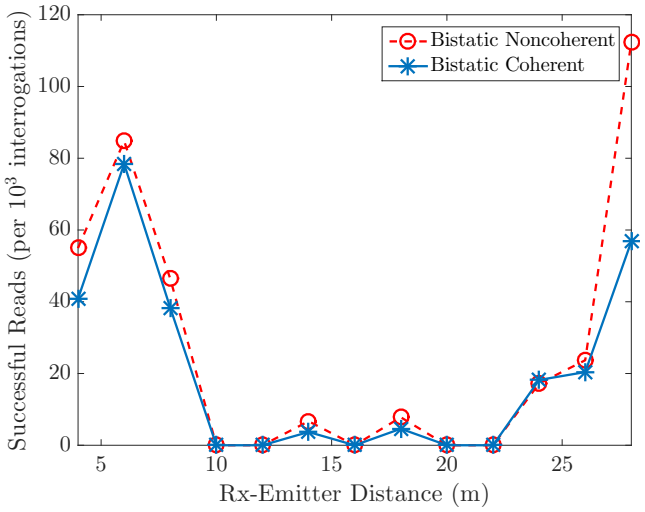

Fig. 14. Successful RFID tag reads versus Rx-Emitter distance in the bistatic setup of Fig. 13, with the noncoherent scheme of Sec. V and coherent detector of Sec. IV. The proposed noncoherent scheme outperforms, in terms of successful reads, the coherent counterpart for all distance setups. This experimental result validates the striking simulation result of Fig. 9. The CFO correction being imperfect breaks the flat fading assumption and thus, hinders the CSI estimation and coherent detection performance. On the other hand, the robustness of the proposed noncoherent algorithm is further demonstrated.

industrial equipment, for various different values of transmission power. An MTI MT-242032 7 dBi antenna was connected to the reader through a 0.504 dB loss coaxial cable. Two different Gen2 tags, namely, Alien ALN-9741 (Higgs-4) and Alien ALN-9540 (Higgs-2), were tested with similar results in terms of reading range and rate. In the case of 15 dBm Tx power, the reader was able to interrogate the tags at a distance of 1.1 m, while at 30 dBm, the reading distance increased to 4.5 m. It is also noted that the reader antenna was placed at 0.9 m above the ground, relatively close to the ground.

The purpose of the above test, was to discover the sector radius under which the tags could operate.[3] This means that, by utilizing more Tx SDRs in a given space, the coverage increases, thus the probability of a tag being in the vicinity of an illuminating source is greater.

Fig. 10 examines how a multistatic topology can increase coverage. Three Ettus N200 SDRs were utilized with FLEX 900 daughter-cards, two for Tx and one for Rx; the Tx power was set to 15 dBm; Tx SDRs were connected to the aforementioned 7 dBi antennas, through 0.45 dB loss cables, while the Rx SDR was connected to an MT-242017, 10 dBi antenna, through an 0.504 dB loss coaxial cable. All SDRs were connected to an HP Procurve 2824 Ethernet switch, with 15 m-long, Cat5e cables. The host PC running the software responsible for baseband processing and handling the SDRs was also connected on the Ethernet switch. The two Tx SDRs operate in a time division multiplexing fashion, while any sort of scheduling could be possible, even for additional SDRs. In Fig. 10 there were two tags, each located in the sector radius of a single Tx SDR. Tag A (ALN-9540) is 70 cm away from Tx-2, and Tag B (ALN-9741) is 1.1 m away from Tx-1. Receiving SDR was 2.6m and 4.7m away from Tx-2 and Tx-1, respectively. When Tx-1 was active (and Tx-2 inactive) the reader would interrogate only Tag B, and vice-versa. This showcases what was previously stated: more Tx SDRs means that there is a greater chance that a tag will be in the sector radius of an illuminating source to satisfy the RF harvesting sensitivity limitations.

Further developing on the idea of a multistatic reader, it is intuitively expected that the larger the deployment of emitters in a given area, the more likely it is for a tag to be powered on and be successfully interrogated. Experiments were carried out to assess the above and study the coverage offered by monostatic (using a Thing Magic Sargas RFID reader), bistatic and multistatic setups. In all cases, MT-242032/NRH antennas were used. The output power of the commercial reader was set at 24 dBm. Using a Mini-Circuits ZRL-1200+ amplifier, the same output power was configured on the USRP acting as emitter. The minimum BLF allowed by the commercial reader was 250 kHz, and 40 kHz for the SDR reader, while Miller-2 line code was used. A grid of 32 positions was considered for the experiment, in an area of ≈ 13 m^2 (Fig. 11). For the monostatic case, the commercial reader was placed at position "Tx 1", while for the bistatic and multistatic cases, the USRP acting as the receiver was placed in the spot denoted by "Rx" in Fig. 12. For the bistatic case, the USRP acting as the emitter was placed in spot "Tx 1". In the multistatic case, the second emitter was placed in the spot denoted as "Tx 2".

As it can be seen in Fig. 11, a multistatic setup clearly covers a greater area (denoted by the outlines around the RFID positions) as the RFID was successfully interrogated at 24 out of the 32 available positions, representing a coverage of $\approx$ 9 m^2. Under a monostatic setup, the tag could be interrogated at 12 (≈ 4 m^2) positions, while in the bistatic at 14 (≈ 5 m^2). Notice that in the specific setup, the multistatic architecture roughly doubled the RFID coverage, compared to monostatic. The area gain offered by the bistatic/multistatic setup (compared to monostatic) is explained by the inherent Tx/Rx channel asymmetry and independence [3].

In order to further demonstrate the modular nature of this setup and feasibility of low-cost implementation, a 7 $ RTL-SDR dongle (connected via USB to the PC) replaced

[3]Note the directivity of the antenna defines a sector outside of which, the tags are not illuminated at all.

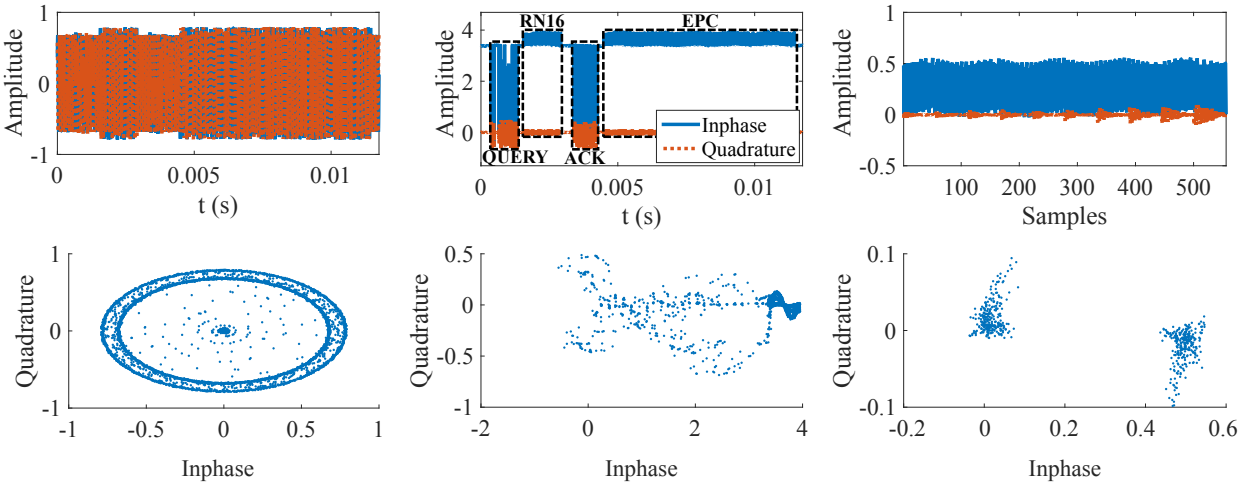

Fig. 15. Experimental waveforms (Top) & scatter plots (Bottom) of the received samples, from the testbed. Received samples prior to CFO compensation (Left), after CFO compensation (Middle) and after CFO-DC compensation & synchronization (Right).

the Rx SDR. The RTL-SDR was able to interrogate both tags successfully. However, reduced tag reading rates where observed, mainly due to the large buffer size of the RTL, in conjunction with low transfer speed of USB 2.0 (versus 1Gbit Ethernet of N200).

The limiting factor of passive tags is the transmitter-to-tag link. The second setup (see Fig. 13) highlights this limitation, which is inherent in monostatic Gen2 RFID readers. A tag (ALN-9741) was placed 90 cm away from the Tx SDR (USRP N200) and the Rx SDR (both N200 & RTL-SDR) was placed 30 m away from the Tx SDR. The tag was successfully interrogated, which validates the limitation imposed by the transmitter-to-tag link.

Elaborating further on the importance and robustness of the suggested noncoherent scheme in a bistatic scenario, the simulated results of Fig. 9 were validated using the setup of Fig. 13. The experimental results can be seen in Fig. 14. The nature of the Gen2 protocol makes it complicated to decouple the EPC BER from the RN16 BER, since receiving an EPC packet requires correct decoding of the RN16 packet. Note that the RN16 cannot be used for BER estimation, since it is a random 16-bit sequence, unknown to the reader. Thus, the number of successful RFID tag reads was used as a benchmark for the bit error rate. Additionally, the distance between the Rx and Tx antennas was used as a proxy for the SNR. Examination of Fig. 14 reveals that the proposed noncoherent scheme outperforms the coherent in terms of successful reads for all Rx-Emitter distances. The performance gap between the two methods is attributed to the imperfect CFO correction. The residual CFO breaks the flat fading assumption and thus, CSI estimation and coherent sequence detection underperform. Instead, we see that the noncoherent scheme is robust to that residual CFO, and thus more suitable for a bistatic scenario, with improved performance (e.g., the read-rate is almost doubled at distance of 28 m). Observe that for some of the distances the number of reads is close or equal to 0. This is because of destructive multipath interference that occurs for each such distance setup. Finally, note that the curve of Fig. 14 doesn't have a decreasing trend as the distance increases. This can also be explained by the multipath propagation that might lead to either constructive of destructive interference.

For completeness purposes, Fig. 15 demonstrates the various processing stages of the samples received from a bistatic setup, similar to Fig. 13. Inphase and quadrature plots, before CFO compensation, after CFO compensation and after CFO compensation, DC removal and symbol level synchronization, are also depicted. This work tests the proposed detector, following a holistic approach, as needed in practice. All setups, using either USRP or RTL-SDR, were tested using both coherent and noncoherent sequence detection schemes (see Sec. IV & V) and the performance was similar, with respect to tag reading rate. Thus, simulation results were validated; furthermore, substantial evidence was offered that the PLL can effectively address the CFO problem; finally, it was shown that the proposed noncoherent scheme performs on par with coherent schemes (BER-wise), in realistic scenarios.

Finally, it is noted that the utilized BLF in the system was the lowest possible, i.e., 40 kHz. However, BLF is not limited by the detection schemes, but rather by the computational power of the PC and the delay introduced by sample transferring between the SDRs and the PC. It is emphasized that the proposed noncoherent detection scheme offers linear complexity (to the sequence length), $\mathcal{O}(N)$, as it is a modification of the Viterbi algorithm. Linear complexity is the lowest possible, since at least N decisions must be made for N symbols.

VII. Conclusion

This works fills a gap in the literature concerning near-optimal and time-efficient algorithms for noncoherent sequence detection for industrial Miller 2, 4, 8 line codes. It also validates the performance of the proposed algorithm using both simulation and experimental results, demonstrating practical use and implementation feasibility. In addition to that, this work not only proposes an inexpensive Ethernet- & SDR-based multistatic architecture for tag interrogation, but also

provides experimental validation of the aforementioned setup. The above results offer an inexpensive, modular and robust multistatic RFID/IoT interrogating architecture. Future work will study other connecting physical layers between emitting SDRs (e.g., USB3), distributed beamforming techniques, as well as concrete steps towards convergence of RFID, Ethernet and next generation cellular radio architectures.

ACKNOWLEDGMENT

The authors would like to thank Konstantinos Skyvalakis for his assistance in the experimental results campaign.

REFERENCES

[1] *EPC Radio-Frequency Identity Protocols, Class-1 Generation-2 UHF RFID Protocol for Communications at 860 MHZ-960 MHZ.* EPC Global, 2015, version 2.0.1.

[2] P. N. Alevizos, Y. Fountzoulas, G. N. Karystinos, and A. Bletsas, "Log-linear-complexity GLRT-optimal noncoherent sequence detection for orthogonal and RFID-oriented modulations," *IEEE Trans. Commun.*, vol. 64, no. 4, pp. 1600–1612, Apr. 2016.

[3] P. N. Alevizos, K. Tountas, and A. Bletsas, "Multistatic scatter radio sensor networks for extended coverage," *IEEE Trans. Wireless Commun.*, vol. 17, no. 7, pp. 4522–4535, Jul. 2018.

[4] P. N. Alevizos and A. Bletsas, "Non-linear far field RF harvesting in wireless communications," *IEEE Trans. Wireless Commun.*, vol. 17, no. 6, pp. 3670–3685, Jun. 2018.

[5] M. Buettner and D. Wetherall, "A software radio-based UHF RFID reader for PHY/MAC experimentation," in *Proc. IEEE RFID*, Apr. 2011, pp. 134–141.

[6] G. D. Durgin, "RF thermoelectric generation for passive RFID," in *Proc. IEEE RFID*, Orlando, FL, May 2016, pp. 1–8.

[7] J. F. Ensworth and M. S. Reynolds, "Every smart phone is a backscatter reader: Modulated backscatter compatibility with bluetooth 4.0 low energy (BLE) devices," in *Proc. IEEE RFID*, San Diego, CA, Apr. 2015, pp. 78–85.

[8] J. F. Ensworth and M. S. Reynolds, "BLE-Backscatter: Ultralow-Power IoT Nodes Compatible With Bluetooth 4.0 Low Energy (BLE) Smartphones and Tablets," *IEEE Transactions on Microwave Theory and Techniques*, vol. 65, no. 9, pp. 3360–3368, Sep. 2017.

[9] Y. Fountzoulas, D. Chachlakis, G. N. Karystinos, and A. Bletsas, "GLRT-optimal blind MSK detection with log-linear complexity," in *2016 23rd International Conference on Telecommunications (ICT)*, May 2016, pp. 1–5.

[10] Z. Fu, M. J. Crisp, S. Yang, R. V. Penty, and I. H. White, "Long distance passive UHF RFID system over ethernet cable," in *Proc. IEEE RFID Techn. and Applications (RFID-TA)*, Warsaw, Poland, Sep. 2017, pp. 294–298.

[11] J. D. Griffin and G. D. Durgin, "Gains for RF tags using multiple antennas," *IEEE Trans. Antennas Propagat.*, vol. 56, no. 2, pp. 563–570, Feb. 2008.

[12] V. Iyer, V. Talla, B. Kellogg, S. Gollakota, and J. Smith, "Inter-technology backscatter: Towards internet connectivity for implanted devices," in *Proc. ACM SIGCOMM*, Florianopolis, Brazil, 2016, pp. 356–369.

[13] N. Kargas, F. Mavromatis, and A. Bletsas, "Fully-coherent reader with commodity SDR for Gen2 FM0 and computational RFID," *IEEE Wireless Commun. Lett.*, vol. 4, no. 6, pp. 617–620, Dec. 2015.

[14] S. M. Kay, *Fundamentals of statistical signal processing. [Volume I]. , Estimation theory*. Upper Saddle River (N.J.): Prentice Hall, 1993.

[15] J. Kimionis, A. Bletsas, and J. N. Sahalos, "Increased range bistatic scatter radio," *IEEE Trans. Commun.*, vol. 62, no. 3, pp. 1091–1104, Mar. 2014.

[16] ——, "Bistatic backscatter radio for tag read-range extension," in *Proc. IEEE RFID Techn. and Applications (RFID-TA)*, Nice, France, Nov. 2012.

[17] ——, "Design and implementation of RFID systems with software defined radio," in *Proc. IEEE European Conf. on Antennas and Propagation (EuCAP)*, Prague, Czech Republic, Mar. 2012, pp. 3464–3468.

[18] ——, "Bistatic backscatter radio for power-limited sensor networks," in *Proc. IEEE Global Commun. Conf. (Globecom)*, Atlanta, GA, Dec. 2013, pp. 353–358.

[19] V. Liu, A. Parks, V. Talla, S. Gollakota, D. Wetherall, and J. R. Smith, "Ambient backscatter: Wireless communication out of thin air," in *Proc. ACM SIGCOMM*, Hong Kong, China, Aug. 2013, pp. 39–50.

[20] Y. Ma, N. Selby, and F. Adib, "Drone relays for battery-free networks," in *Proc. ACM SIGCOMM*, Los Angeles, CA, 2017.

[21] I. Motedayen-Aval and A. Anastasopoulos, "Polynomial-complexity noncoherent symbol-by-symbol detection with application to adaptive iterative decoding of turbo-like codes," *IEEE Transactions on Communications*, vol. 51, no. 2, pp. 197–207, Feb 2003.

[22] M. Ouroutzoglou and A. Bletsas, "Linear complexity noncoherent Miller sequence detection for batteryless RFID/IoT," in *Proc. IEEE Int. Conf. Communications*, Shanghai, P.R. China, May 2019.

[23] M. Ouroutzoglou, A. Bletsas, and G. N. Karystinos, "Intelligent non-coherent sequence equals coherent detection: Experimental proof in industrial RFID," in *7th International Conference on Modern Circuits and Systems Technologies (MOCAST)*, May 2018, pp. 1–4.

[24] M. Ouroutzoglou, G. Vougioukas, P. N. Alevizos, A. G. Dimitriou, and A. Bletsas, "Multistatic Gen2 RFID over Ethernet with Commodity SDRs," in *Proc. IEEE RFID Techn. and Applications (RFID-TA)*, Sep. 2019, submitted, under review.

[25] A. Polydoros and K. M. Chugg, "Per-Survivor Processing (PSP)," in *Wireless Communications: TDMA versus CDMA*. Boston, MA, USA: Springer, 1997, pp. 41–72.

[26] R. Raheli, A. Polydoros, and C.-K. Tzou, "Per-Survivor Processing: A General Approach to MLSE in Uncertain Environments," *IEEE Trans. Commun.*, vol. 43, pp. 354 – 364, Feb./Mar./Apr. 1995.

[27] M. Rice, *Digital Communications: A Discrete-time Approach*. Pearson/Prentice Hall, 2009.

[28] R. Sadr *et al.*, "RFID systems using distributed exciter network," Mar. 2013, US Patent 8,395,482 B2. [Online]. Available: https://patents.google.com/patent/US8395482B2/en?oq=US8395482

[29] M. Simon and D. Divsalar, "Some interesting observations for certain line codes with application to RFID," *IEEE Trans. Commun.*, vol. 54, no. 4, pp. 583–586, April 2006.

[30] V. Talla, M. Hessar, B. Kellogg, A. Najafi, J. R. Smith, and S. Gollakota, "Lora backscatter: Enabling the vision of ubiquitous connectivity," *Proc. ACM Interact. Mob. Wearable Ubiquitous Technol.*, vol. 1, no. 3, pp. 105:1–105:24, Sep. 2017. [Online]. Available: http://doi.acm.org/10.1145/3130970

[31] D. Chachlakis, "Optimal noncoherent trellis decoding," Diploma thesis available in: https://dias.library.tuc.gr/view/66126, School of ECE, Technical University of Crete, Chania, Greece, Jul. 2016, Supervisor G. N. Karystinos.

[32] E. Stratigi, "Synchronization, channel estimation and detection of RFID signals with Miller coding," Diploma thesis available in: http://dias.library.tuc.gr/view/72071, School of ECE, Technical University of Crete, Chania, Greece, Feb. 2018, Supervisor A. Bletsas.

Michail Ouroutzoglou received a 5 year Diploma in Electrical and Computer Engineering from the Technical University of Crete, Greece, in July 2019. He is currently pursuing his Ph.D. degree at the Electrical Engineering and Computer Science department of MIT. He has worked on wireless communications, signal processing for backscatter communications, and design and implementation of software defined radios and algorithms. As a Ph.D. student, his research lies on the intersection of machine learning and telecommunications where he develops AI-powered wireless systems for health related applications. He was a co-recipient of the 2018 IEEE International Conference on Modern Circuits and System Technologies (MOCAST) Best Student Paper Award on Communications. Contact: michail@mit.edu

Georgios Vougioukas received the 5-year Diploma degree in Electrical and Computer Engineering, in 2016 and the Ph.D. degree in 2020, from Technical University of Crete (TUC), Greece. His research interests include methods for ultra-low power wireless communication, signal processing for backscatter communication, energy harvesting, sensing, analog & digital system design and implementation. He was co-recipient of the 2017 IEEE International Conference on RFID Technology & Applications (RFID-TA) Best Student Paper Award. He has been distinguished as Exemplary Reviewer for 2017 by the Editorial Board of IEEE Transactions on Wireless Communications. Contact: gevougioukas@isc.tuc.gr

George N. Karystinos was born in Athens, Greece, in 1974. He received the Diploma degree in computer science and engineering (five-year program) from the University of Patras, Patras, Greece, in 1997, and the Ph.D. degree in electrical engineering from The State University of New York at Buffalo, Amherst, NY, USA, in 2003. From 2003 to 2005, he held an Assistant Professor position with the Department of Electrical Engineering, Wright State University, Dayton, OH, USA. Since 2005, he has been with the School of Electrical and Computer Engineering, Technical University of Crete, Chania, Greece, where he is currently a Professor. He served as an expert in the Programme Committee of ERC, FET, and MSCA within the European Commission's Horizon2020 Framework Programme from 2019 to 2021. Since 2021, he is a National Representative to the Horizon Europe Programme Committee for MSCA.

Prof. Karystinos' research interests include communication theory and signal processing with emphasis on signal design, receiver optimization, channel coding, and physical-layer security. For articles that he coauthored with students and colleagues, he received a 2001 IEEE International Conference on Telecommunications Best Paper Award, the 2003 IEEE Transactions on Neural Networks Outstanding Paper Award, the 2011 IEEE International Conference on RFID-Technologies and Applications Second Best Student Paper Award, the 2013 International Symposium on Wireless Communication Systems Best Paper Award in Signal Processing and Physical Layer Communications, the 2015 IEEE International Conference on Acoustics, Speech, and Signal Processing Best Student Paper Award, and the 2018 IEEE International Conference on Modern Circuits and Systems Technologies Best Student Paper Award.

Aggelos Bletsas received the Diploma degree (with honors) in Electrical and Computer Engineering from Aristotle University of Thessaloniki, Greece in 1998, and the M.Sc. and Ph.D. degrees from MIT, Cambridge, MA, USA, in 2001 and 2005, respectively. He has worked at Mitsubishi Electric Research Laboratories (MERL), Cambridge, MA and RadioCommunications Laboratory (RCL), Department of Physics, Aristotle University of Thessaloniki. He currently serves as full Professor, School of Electrical & Computer Engineering, Technical University of Crete, Greece. His research interests span the broad area of scalable wireless communications and sensor networking, with emphasis on ultra-low power/cost environmental sensing, backscatter radio and ambiently-powered inference networks. His current focus and contributions are relevant to wireless, batteryless, backscatter sensors for precision agriculture that cost a few Euros, consume a few microWatts and can be read with commodity receivers and smartphones. He has served as Associate Editor of *IEEE Transactions on Wireless Communications* (2015-2021) and *IEEE Wireless Communications Letters* (from foundation in 2011-2016) and Technical Program Committee (TPC) member of major IEEE conferences. Dr. Bletsas was co-recipient of the *IEEE Communications Society 2008 Marconi Prize Paper Award in Wireless Communications*, and various Best Student Paper Awards e.g., in IEEE RFID-TA 2011, IEEE ICASSP 2015, IEEE RFID-TA 2017, MOCAST 2018. He has been included in the Highly-Cited Greek Scientists list. One of his papers is ranked 1st in Google Scholar *Classic Papers in Computer Networks & Wireless Communication*.